JOURNAL OF THERMOPHYSICS AND HEAT TRANSFER
Vol. 25, No. 2, April–June 2011

Computation of Segmented Arc-Heater Flows Considering Injection of Electrode Shield Gas

Jeong Il Lee*
University of Stuttgart, 70569 Stuttgart, Germany
and
Garam Jeong† and Kyu Hong Kim‡
Seoul National University, Seoul 151-742, Republic of Korea

DOI: 10.2514/1.50774

The computer code ARCFLO4, used to solve segmented arc-heater flows, is improved to consider argon gas injected into the electrode chambers and air injected from the constrictor wall. The additional species continuity equation for argon gas including the diffusion term is solved with the original governing equations for total working gas. Also, a numerical wall boundary condition, wherein air is injected from small gaps between constrictor disks, is applied to predict heat flux more realistically. This code is used to simulate flows at the Panel Test Facility, the Aerodynamic Heating Facility, and the Interaction Heating Facility of the NASA Ames Research Center. The computations show that the argon ratio changes dramatically in the arc heater, and it strongly influences the distribution of the thermodynamic and transport properties of the flow. At the upstream region of the constrictor, the arc column is broad and the radiation increases. In addition, a periodic distribution of conductive heat flux on the constrictor wall occurs along the axial direction due to gas injected from gaps between the constrictor disks. The average heat flux on the disk is higher than the previous result that considered working gas with a fixed argon ratio. Finally, through comparison between computation and experiment, it is confirmed that the proposed computation effectively predicts the total heat flux on the arc heater.

Nomenclature

c_{Ar} = mass fraction of argon gas
c_i = mass fraction of species
$c_{p,i}$ = specific heat of species at constant pressure, J/kg · K
D_{Ar} = effective diffusion coefficient of argon gas, m^2/s
D_{ij} = multicomponent diffusion coefficient, m^2/s
D_{im} = effective binary diffusion coefficient, m^2/s
E = voltage gradient, V/m
e_t = total internal enthalpy, J/kg
H = total enthalpy, J/kg
H_a = mass-averaged enthalpy, J/kg
H_c = centerline enthalpy, J/kg
I = current, A
j = current density, A/m^2
k = Boltzmann constant, 1.380622×10^{-23} J/K
L = length of constrictor, m
M_i = molecular weight of species i, kg/kg · mole
N_s = total number of species
n_i = number density of species i, m^{-3}
p = pressure, Pa
q_C = conductive heat flux, W/m^2
q_R = radiative heat flux, W/m^2
R = universal gas constant, 8314.3 J/kg · mole · K
T = temperature, K
u = axial velocity, m/s
V = voltage, V
v = radial velocity, m/s
x = axial coordinate, m
y = radial coordinate, m
η = arc-heater efficiency
ρ = density, kg/m^3
τ_{ij} = stress tensor, N/m^2

Presented as Paper 2009-0456 at the 47th AIAA Aerospace Sciences Meeting, Orlando, FL, 5–8 January 2009; received 16 May 2010; revision received 2 November 2010; accepted for publication 23 December 2010.

*Postdoctoral Fellow, Institute of Space Systems, Pfaffenwaldring 31; snow0730@empal.com. Member AIAA.

†Graduate Research Assistant, School of Mechanical and Aerospace Engineering, Sillim-Dong, Gwanak-Gu, Seoul; sadadjr@naver.com. Member AIAA.

‡Associate Professor, School of Mechanical and Aerospace Engineering and Institute of Advanced Aerospace Technology, Sillim-Dong, Gwanak-Gu; aerocfd1@snu.ac.kr. Member AIAA (Corresponding Author).

I. Introduction

AN ARC-JET wind tunnel generates the flow environment that a vehicle experiences when traversing the atmosphere of a planet. It is primarily used to test heat shield materials and thermal protection system components for planetary entry vehicles and hypersonic flight vehicles. An arc heater is a key device for this type of wind tunnel, which produces high enthalpy flow directly by arc heating. Among several types of arc heaters, segmented arc heaters are widely used because they produce stable flow under a wide range of operating conditions. A segmented arc heater consists of an anode chamber, a constrictor tube, a cathode chamber, and a nozzle, as shown in Fig. 1. A test gas is injected through the wall of the constrictor, and a shield gas is injected from the wall of the electrode chambers. An arc spans between the two electrodes and heats the core gas in the constrictor. The surrounding gas is heated by radiation emitted from the core gas and by turbulent mixing. Finally, the high-temperature gas exits through the nozzle into the test section.

We numerically evaluated the flow physics in an arc heater and designed a new arc heater with enhanced efficiency. Historically, many numerical investigations have been carried out with this purpose. In the 1970s, Nicolet et al. [1] developed the ARCFLO code based on the work of Watson and Pegot [2]. However, the applicability of the ARCFLO code was quite restrictive in the actual design or development of arc heaters because it employed the space marching technique, which requires knowledge of upstream conditions in advance. Therefore, to overcome this shortcoming, Kim et al. [3] developed a time-marching code, ARCFLO2, that retained the two-band radiation model and the algebraic turbulence model from the ARCFLO code. With this code, flows of some arc

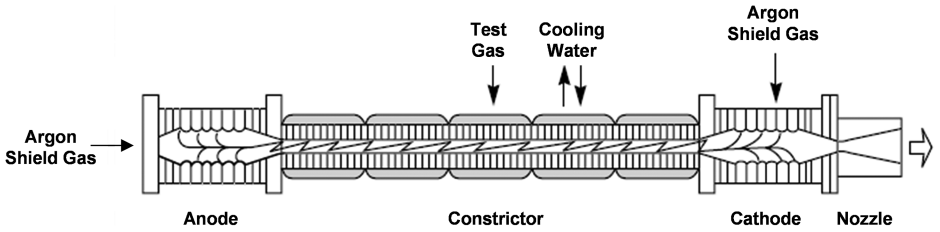

Fig. 1 Schematic drawing of segmented arc heater.

heaters were simulated successfully only with given conditions of current and mass flow rate. Subsequently, Sakai and Olejniczak [4,5] and Sakai [6] tried to improve the numerical modeling of ARCFLO and ARCFLO2. They developed a new three-band radiation model that was quite consistent with a detailed line-by-line calculation; this code was named ARCFLO3. However, ARCFLO3 and ARCFLO2 did not always provide acceptable accuracy for the various arc heaters because of inaccurate prediction of turbulence phenomenon. Lee et al. [7–10] developed an improved numerical code, ARCFLO4, that can be applied to the various arc heaters under arbitrary operating conditions. Instead of a conventional algebraic turbulence model, a two-equation turbulence model that is able to express the convective physics of turbulence and does not explicitly demand a mixing length was adopted. Also, the three-band radiation model of ARCFLO3, for which the performance and numerical accuracy were already proven by Sakai and Olejniczak [5], was used. It was observed that the k-ε turbulence model [11] combined with the three-band radiation model provided the most accurate solutions, especially for arc-heater operational data, over a diverse range of operating conditions.

A main purpose of this study is to improve the accuracy of heat flux prediction using the recent ARCFLO4 code. To design a new segmented arc heater, it is very important to know the heat flux on the interior wall of the arc heater and to predict the operational data. Accurate prediction of the heat flux contributes to the determination of a detailed arc-heater configuration and the size of a cooling system. Taunk et al. [12] measured interior wall heat flux using a calorimeter and simulated the flows using the ARCFLO code. Sakai and Olejniczak [4,5] also computed flows under the same flow conditions using the ARCFLO3 code and compared the computational data with Taunk et al.'s [12] experimental data. The ARCFLO3 code could effectively predict the total heat flux at the downstream region of the arc heater, but it considerably underestimated the flux at the upstream region. The computation using the previous ARCFLO4 code also underestimated the heat flux at the upstream region, although the computation for the operational data agreed very well with the experimental results. Among several possibilities for this underestimation, the assumption of a fixed argon ratio in the flow was suspected as the primary reason. In the experiments, a small amount of argon was injected into the anode chamber, flowed along the stream in the constrictor, and was gradually mixed with air injected from the constrictor wall. Thus, in reality, the ratio of argon to the total working gas was changeable along the stream in the arc heater. However, until now, all previous computations treated the working gas as a mixture with the fixed argon ratio or pure air. In a previous study [10], Lee et al. confirmed that as the fixed argon ratio in the working gas increased, the arc column (i.e., the high-temperature region around the core) became thicker. Thus, radiation was enhanced toward the wall. Realistically, it is certain that the argon ratio stayed very high from the anode to the upstream region of the constrictor. Therefore, if a realistic argon ratio is considered in the computations, the total heat flux becomes higher at the upstream region of the arc heater.

To apply these observations on the actual argon ratio to flow simulations, the continuity equation of argon gas with the diffusion term was solved. Also, the thermodynamic and transport properties of the mixture including Ar and Ar^+ were computed under the assumption of thermal equilibrium. These numerical approaches were used to simulate flows of the Panel Test Facility (PTF), the Aerodynamic Heating Facility (AHF), and the Interaction Heating Facility (IHF) at the NASA Ames Research Center [13].

This remainder of the paper is organized as follows. Section II briefly describes our numerical and physical modeling, including the governing equations and boundary conditions. In Sec. III, we describe how PTF, AHF, and IHF flows were simulated to verify the performance of the proposed numerical approaches, and the role of the argon gas is investigated. Concluding remarks are presented in Sec. IV.

II. Numerical Modeling

A. Governing Equations

Generally, the flow in a segmented arc heater is a complex plasma flow that is heated directly by an arc. The temperature of the core gas in the constrictor is higher than 10,000 K. Thus, the flow includes many ions and electrons as well as atoms and molecules. Because of high-temperature flow around the core, the radiation transfers a significant amount of heat energy from the core gas to the surrounding gas. Also, the turbulent mixing lets the heat energy move from one region to another region. At the constrictor wall, some heat energy is removed by cooling water circulating through the constrictor disks.

Based on the physics of arc-heated flows, the governing equations are the time-dependent axisymmetric Navier–Stokes equations that include joule heating by arc, radiation, and turbulence, as shown in Eqs. (1–3). Even though nonequilibrium effect cannot be neglected at the core of arc, it may be restricted within the core in the type of segmented constrictor, because pressure is high in constrictor and the fluctuation of arc is much smaller in space and time than other types of arc heater. Thus, the working gas in a constrictor was assumed to be in a chemical equilibrium state [1–6]. In addition, to reflect the separated injection of air and argon, it was treated as a mixture of air and argon in the present paper, and the continuity equation of argon gas with a diffusion term was added to the governing equations.

The argon gas included both neutral and ionized argon, and the thermodynamic and transport properties of mixing gas were calculated by considering 11 species, including Ar and Ar^+ (N_2, O_2, Ar, N, O, NO, Ar^+, N^+, O^+, NO^+, and e^-). In Eq. (2), the total density ρ for the working gas means the sum of densities for air and argon. The density of air ρ_{air} was calculated by subtracting argon gas density ρ_{Ar} from the total working gas density ρ:

$$\frac{\partial \mathbf{Q}}{\partial t} + \frac{\partial \mathbf{E}}{\partial x} + \frac{\partial \mathbf{F}}{\partial y} + \mathbf{H} = \frac{\partial \mathbf{E}_v}{\partial x} + \frac{\partial \mathbf{F}_v}{\partial y} + \mathbf{H}_v + \mathbf{I} \tag{1}$$

$$\mathbf{Q} = \begin{bmatrix} \rho \\ \rho_{\text{Ar}} \\ \rho u \\ \rho v \\ \rho e_t \end{bmatrix}, \quad \mathbf{E} = \begin{bmatrix} \rho u \\ \rho_{\text{Ar}} u \\ \rho u^2 + p \\ \rho uv \\ \rho Hu \end{bmatrix}, \quad \mathbf{F} = \begin{bmatrix} \rho v \\ \rho_{\text{Ar}} v \\ \rho uv \\ \rho v^2 + p \\ \rho Hv \end{bmatrix},$$
$$\mathbf{I} = \begin{bmatrix} 0 \\ 0 \\ 0 \\ 0 \\ -j \cdot E \end{bmatrix}, \quad \mathbf{H} = \frac{1}{y} \begin{bmatrix} \rho v \\ \rho_{\text{Ar}} v \\ \rho uv \\ \rho v^2 + p \\ \rho Hv \end{bmatrix} \tag{2}$$

$$\mathbf{E}_v = \begin{bmatrix} 0 \\ \rho D_{\mathrm{Ar}} \frac{\partial c_{\mathrm{Ar}}}{\partial x} \\ \tau_{xx} \\ \tau_{xy} \\ u\tau_{xx} + v\tau_{xy} - q_{C,x} \end{bmatrix},$$

$$\mathbf{F}_v = \begin{bmatrix} 0 \\ \rho D_{\mathrm{Ar}} \frac{\partial c_{\mathrm{Ar}}}{\partial y} \\ \tau_{xy} \\ \tau_{yy} \\ u\tau_{xy} + v\tau_{yy} - q_{C,y} - q_R \end{bmatrix}, \tag{3}$$

$$\mathbf{H}_v = \frac{1}{y} \begin{bmatrix} 0 \\ \rho D_{\mathrm{Ar}} \frac{\partial c_{\mathrm{Ar}}}{\partial y} \\ \tau_{xy} \\ \tau_{yy} - \tau_{\theta\theta} \\ u\tau_{xy} + v\tau_{yy} - q_{C,y} - q_R \end{bmatrix}$$

where

$$q_c = q_{\mathrm{tr}} + q_{\mathrm{int}} + \rho \sum_i D_i h_i \frac{\partial c_i}{\partial T}$$

The q_{tr}, q_{int}, and

$$\rho \sum_i D_i h_i \frac{\partial c_i}{\partial T}$$

are translational, internal, and diffusion components, respectively [10].

Numerically, the governing equations were then discretized using the finite volume method. The inviscid flux was given by the AUSMPW+ scheme [14,15]. The viscous flux was calculated through a central difference scheme. The inviscid term was handled implicitly by applying the lower–upper symmetric Gauss–Seidel method [16]. The axisymmetric source, the joule heating, and the viscous term were calculated explicitly. The computational grid, which is scaled up to 10 times in the radial direction, is shown in Fig. 2. A grid with 289×80 cells that has 200 cell points along the surface of the constrictor was usually used, but a grid with 531×80 cells that has 400 cell points along the surface of the constrictor was used for detailed computations of the heat flux. With these grids, L_2 norms of density variations $\|\Delta\rho\|$ were reduced to 10^{-5} for all calculations. The difference in computed operational data between these two grids under the same flow condition is less than 0.5%.

B. Boundary Conditions

In all previous computations [1–10], the working gas was treated as a pure-air or a mixture-with-fixed-argon-ratio case, although an argon gas was injected separately in the case of a real segmented arc heater. In this study, to increase the reality of gas injection, air was supplied from the wall of the constrictor, and argon was injected from the upstream surface of the anode chamber and the wall of the cathode chamber. Furthermore, the air was injected through small gaps regularly spaced along the constrictor wall in the case of a real segmented arc heater. Thus, the inner surface between starting and end points of the constrictor was divided into a gap and a wall surface for a more realistic boundary condition, as shown in Fig. 3. The ratio of the gap area to the total constrictor wall area was chosen to be 20%

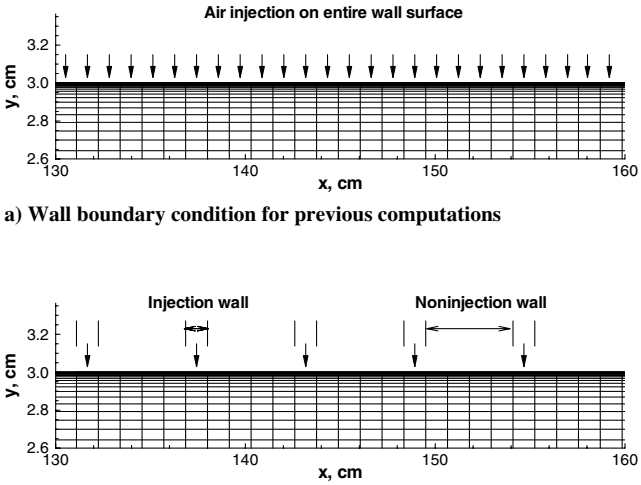

a) Wall boundary condition for previous computations

b) Wall boundary condition for present computations

Fig. 3 Descriptions of wall boundary conditions for test gas injection.

after grid convergence tests were performed. The details are explained at Sec. III.

The wall density was determined by the equilibrium relation between the wall temperature and pressure. The outlet condition was extrapolated from the value of the inner computational domain since the region after the nozzle throat was supersonic. The values of the properties on the symmetric axis were obtained from the symmetric condition.

C. Equilibrium Composition, Thermodynamic Properties, and Transport Properties

To obtain the thermodynamic and transport properties of a mixture, information of the equilibrium composition and the individual species properties are essential. The concentrations of the individual species were obtained from the Gibbs free-energy-minimization calculation procedure [17], which can treat each species independently without specifying a set of reactions a priori. The present calculations were based on an 11-species model including Ar and Ar^+ (N_2, O_2, Ar, N, O, NO, Ar^+, N^+, O^+, NO^+, and e^-). The individual species properties were obtained from the recent NASA John H. Glenn Research Center at Lewis Field thermodynamic database [18] for a temperature range up to 20,000 K. Thus, the accuracy of computations for the composition of ions and electrons was improved above 10,000 K compared with our previous computations that used the old Joint Army–Navy–Air Force (JANAF) thermodynamic database. With the individual species composition and properties, the thermodynamic properties for the 11-species air–argon mixture model were simply calculated [10,19]. Transport properties of a mixture were computed using the approximate formulations in [19,20] instead of the complete kinetic theory expressions (i.e., the Chapman–Enskog formula) in [21]. They required the data on the collision integral, which is classified into the momentum transfer cross section $\pi\Omega_{ij}^{(1,1)}$ and the viscosity cross section $\pi\Omega_{ij}^{(2,2)}$. Most collision cross sections including the air species were obtained from [22,23]. However, for the ionized species, the effective Coulomb cross section [19,20] was used.

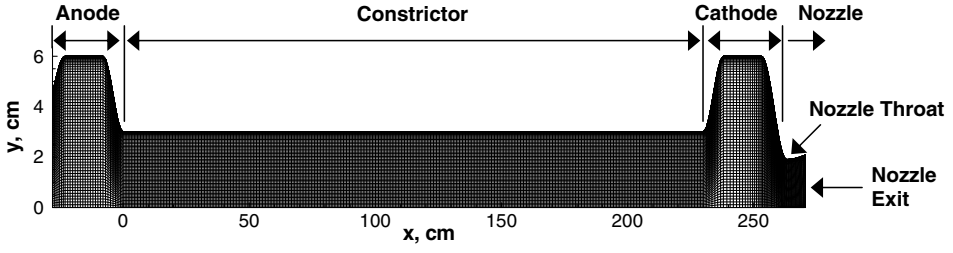

Fig. 2 Grid system of AHF arc heater (289 × 80 mesh).

To solve the continuity equation for the argon gas, the effective binary diffusion coefficient D_{im} is needed. The formula is as follows:

$$D_{im} = \frac{1 - n_i}{\sum_{j=1, j\neq i}^{N_S} n_j / D_{ij}} \tag{4}$$

D_{ij} is an ordinary binary diffusion coefficient computed as follows:

$$D_{ij} = \frac{kT}{p\Delta_{ij}^{(1)}} \tag{5}$$

with

$$\Delta_{ij}^{(1)} = \frac{8}{3}\left[\frac{2M_iM_j}{\pi RT(M_i + M_j)}\right]^{1/2} \pi\Omega_{ij}^{(1,1)} \tag{6}$$

In the preceding computation, the continuity equation for argon gas does not distinguish between neutral argon and ionized argon. Also, we assumed that a spatial gradient of effective binary diffusion was smaller than that of species mass fraction. Thus, the diffusion coefficient for argon gas was derived by merging two species continuity equations for neutral argon and ionized argon as follows:

$$D_{\mathrm{Ar}} = \frac{D_{\mathrm{Arm}}c_{\mathrm{Ar}} + D_{\mathrm{Ar^+}m}c_{\mathrm{Ar^+}}}{c_{\mathrm{Ar}} + c_{\mathrm{Ar^+}}} \tag{7}$$

where the mass fractions of neutral argon and ionized argon were computed, based on their equilibrium composition, which was computed by minimization of the Gibbs free energy formulation [17].

D. Models for Joule Heating, Radiation, and Turbulence

In theory, Joule heating by arc could be obtained by solving Maxwell's equations. However, if the current distribution is known, the calculation can be simplified using Ohm's law. The constrictor wall of the segmented arc heater is insulated electrically; thus, the current in the constrictor is constant. Concerning the electrical conductivity, it is obtained by a curve-fitted function of pressure and temperature. The details were referred to a previous study by Lee et al. [10]. For high-temperature flow, radiation is an important heat transfer mode together with thermal conduction. The radiative heat flux was calculated by integrating the radiative intensity over all directions and several discrete ranges of frequency in cylindrical coordinates. We adopted the three-band radiation model [5] developed by Sakai and Olejniczak. Using this model, we could compute a radiative transport equation 400 times faster than by using a detailed line-by-line calculation [24], without compromising accuracy. Turbulence is regarded as a key phenomenon in segmented arc-heater flows. We adopted the k-ε turbulence model to describe turbulent flow physics in the arc heaters. In previous studies [7–10], the k-ε [11], k-ω [25], and k-ω shear stress transport [26] two-equation turbulence models that can express the convective flow physics of turbulence and do not explicitly require the mixing length were tested. It was observed that the k-ε turbulence model combined with the three-band radiation model was the most appropriate approach to analyzing segmented arc-heater flows.

III. Results

A. Effect of Separated Injection of Argon

Operational experience with the arc heater has shown that argon injected into electrode chambers reduces electrode wear and contributes to the prevention of arcing between constrictor disks and electrode rings. Because of the separated injection of argon and air, the argon ratio of a working gas changes gradually in an arc heater, and it affects the thermodynamic characteristics. To understand the flow physics within an arc heater accurately, we investigated the influence of argon on the arc-heated flows.

Numerical flow analysis of the AHF was performed to investigate the effect of argon. The AHF is operated with a 20 MW segmented arc heater that produces a pressure range of 1 to 9 atm and an enthalpy level of 1 to 33 MJ/kg. The constrictor diameter and length are 0.06 and 2.3 m, respectively, and the nozzle throat diameter is 0.038 m. For this computation, the operating current was 1600 A and the mass flow rate of the working gas was 0.10 kg/s. Air at 0.07 kg/s was injected through the constrictor wall, and argon at 0.015 kg/s was injected into anode and cathode chambers, respectively.

Figures 4 and 5 show the streamline and the distribution of the density ratio of argon to the total working gas in the AHF arc heater. The argon at 0.015 kg/s, which was injected from the upstream surface of the anode chamber, filled the anode chamber and flowed downstream, mainly along the core of the constrictor. Air at 0.07 kg/s, which was injected from the wall of constrictor, flowed along the surface of the constrictor, was pushed toward the core by the newly injected air, and was mixed with the argon around the core. Also, argon at 0.015 kg/s was injected from the wall of the cathode chamber and flowed along the wall of the cathode chamber and the nozzle. For a detailed description, Fig. 6 shows the density ratio of argon to the total working gas along the radial direction at several cross sections of the arc heater. Figure 6a shows the density ratio distribution at the middle section of the anode chamber. It was confirmed that all gas in the anode chamber was argon. Figure 6b shows the density ratio distribution at the beginning, the middle, and

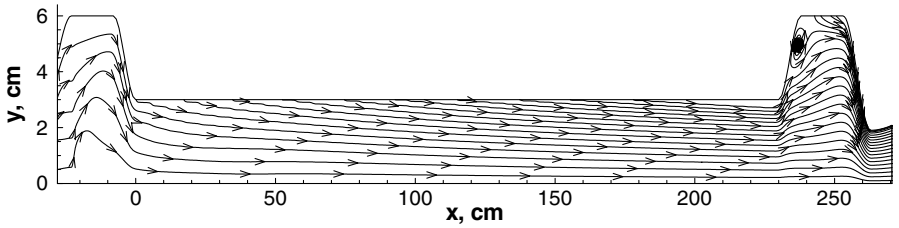

Fig. 4 Streamline in AHF arc heater.

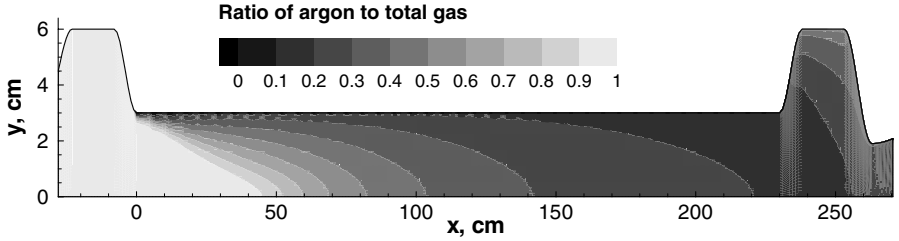

Fig. 5 Distribution of ratio of argon to total working gas in AHF arc heater.

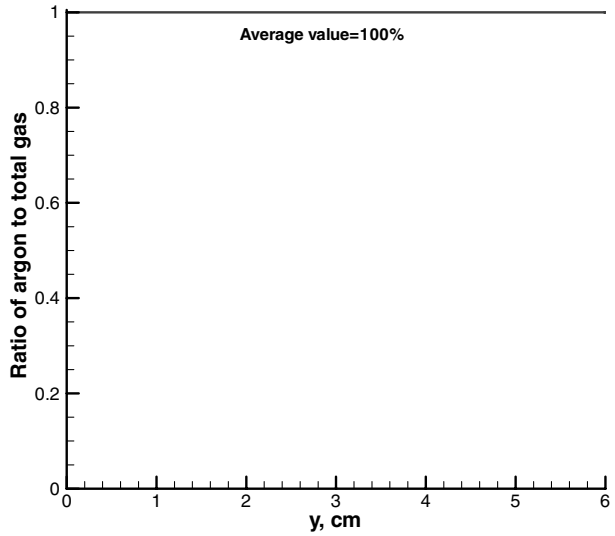

a) Middle section of anode chamber

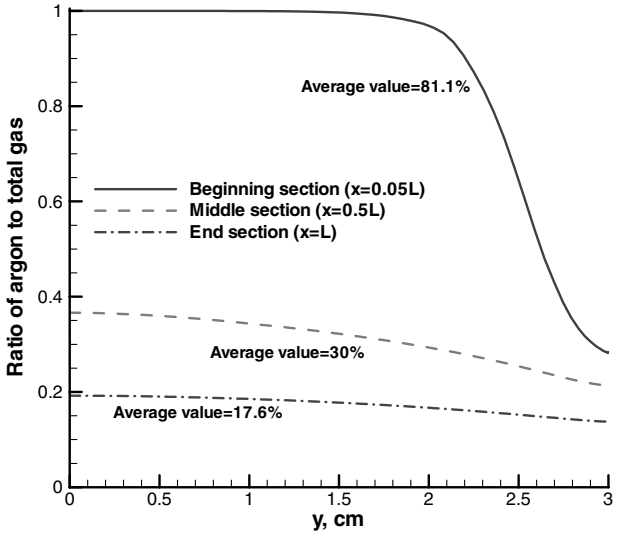

b) Three sections (0.1L, 0.5L, L) in the constrictor

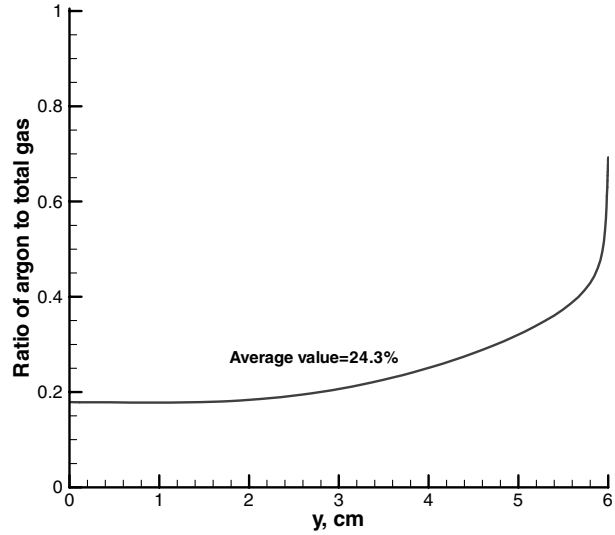

c) Middle section of cathode chamber

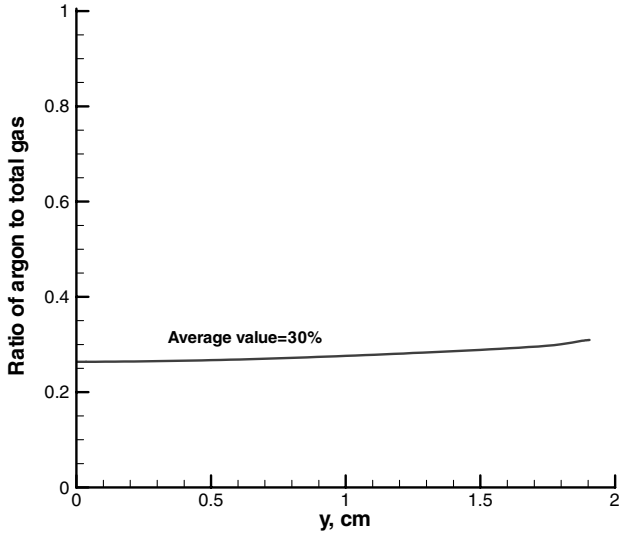

d) Section at the nozzle throat

Fig. 6 Distributions of density ratio of argon to total working gas at cross sections of AHF arc heater.

the end sections of the constrictor. In the beginning section, some air began to be mixed with the argon near the wall by the diffusion phenomenon. After the middle section, the gases mixed rapidly and the argon ratio became nearly 30%, except near the wall. As the gas flowed downstream, the argon ratio decreased because air was injected continuously from the constrictor wall; finally, the ratio became about 17.6% at the end section of the constrictor. Figure 6c shows the density ratio distribution at the middle section of the cathode chamber. The argon ratio increased near the wall because the newly injected argon pushed away the air–argon mixture from the wall, and it was simultaneously mixed with it. Figure 6d shows the density ratio distribution at the nozzle throat. We confirmed that the air and argon were fully mixed at the nozzle throat; thus, the value of the argon ratio was approximately constant.

The enthalpy of argon is much smaller than that of air at the same temperature because the specific heat of argon is lower than that of air. Since the argon ratio is changeable in an arc heater, it is certain that the enthalpy distribution is very different from previous studies [10] that dealt with arc-heated flows with a fixed argon ratio. Figure 7 shows a total enthalpy distribution along the radial direction at the beginning, the middle, and the end cross sections of the constrictor, and the nozzle throat under the same flow condition. The present mixture-with-changeable-argon-ratio case is compared with the previous mixture-with-fixed-argon-ratio case and pure-air case. For the mixture-with-fixed-argon-ratio case, the argon ratio is 30%. In Fig. 7a, the enthalpy for the present computation was the lowest at the beginning region of the constrictor because the argon ratio was very high, as shown in Fig. 6b. As the gas flowed downstream, the amount of air in the flow increased; thus, the enthalpy became higher and approached the enthalpy value for the mixture-with-fixed-argon-ratio case, as shown in Fig. 7b. Here, the average value of the argon ratio is equal to the fixed value (30%) of the mixture-with-fixed-argon-ratio case. In Fig. 7c, the computed enthalpy at the end region of the constrictor is higher than that of mixture-with-fixed-argon-ratio case, because the argon ratio is smaller than that of the mixture-with-fixed-argon-ratio case. As the working gas passed through the cathode chamber, the enthalpy decreased, because new argon gas was injected from the wall of the cathode chamber and arc heating also decreased. After the nozzle throat, both enthalpy distributions were similar, as shown in Fig. 7d, because each average argon ratio was equal to 30%. However, the computed enthalpy for the pure-air case was higher than for the other two cases where argon was considered.

Similar to enthalpy, the temperature distribution was quite different from the previous computational results [10]. Figure 8

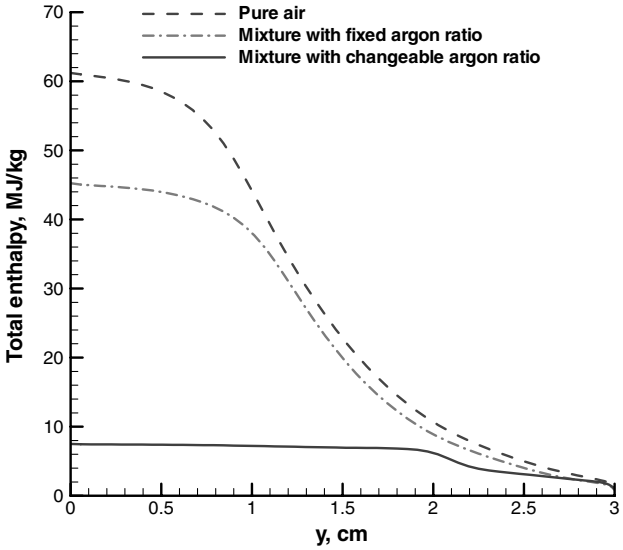

a) Beginning section of constrictor

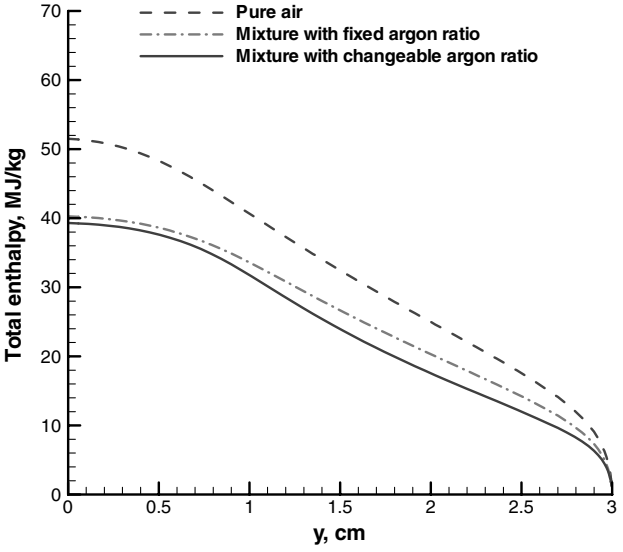

b) Middle section of constrictor

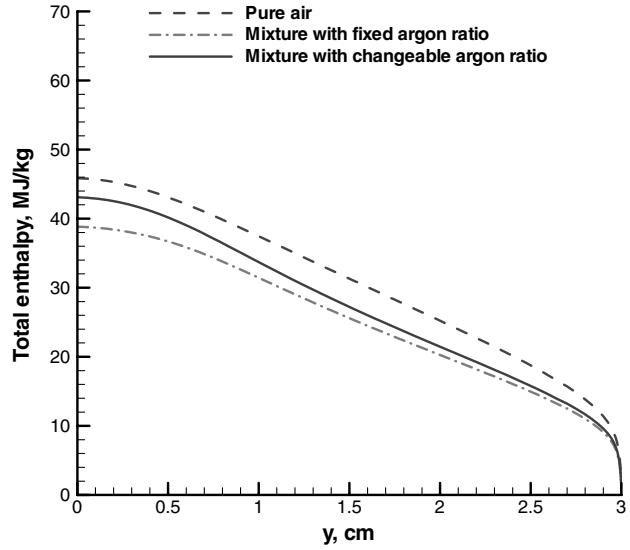

c) End section of constrictor

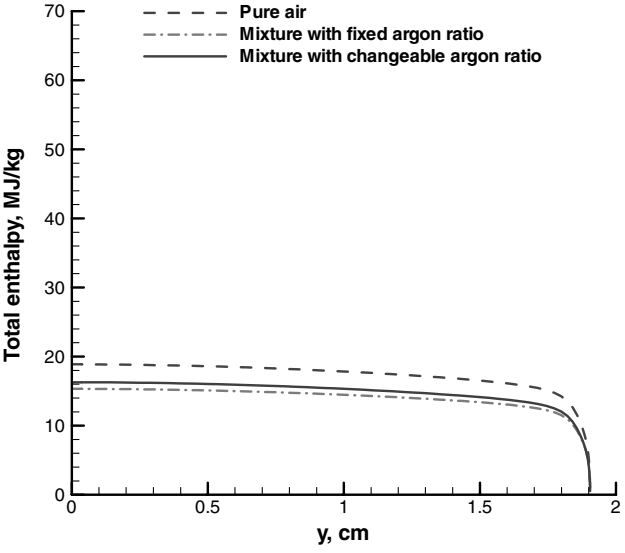

d) Section at nozzle throat

Fig. 7 Enthalpy distributions at cross sections of AHF arc heater.

shows a temperature distribution along the radial direction. At the beginning region of the constrictor, the temperature for the present computation is still higher than 10,000 K around the core, as shown in Fig. 8a, although its enthalpy is much lower than others, as shown in Fig. 7a. The figure also shows that the thickness of the arc column for the present computation is large compared with the previous cases. The thickness of the arc column became larger as the argon ratio increased. After the middle region of the constrictor, the temperature distribution from the present computation became similar to that of the mixture-with-fixed-argon-ratio case, as shown in Figs. 8b and 8c, and the temperatures were higher than those of the pure-air case around the core. Finally, all the temperature distributions became very similar at the nozzle throat, as shown in Fig. 8d.

Based on Figs. 6–8, the change in argon ratio affected temperature and, especially, the total enthalpy. This phenomenon is due to the lower specific heat of argon gas. Generally, the joule heating energy is the greatest at the core of an arc, decreases slightly toward the edge of the arc column, and then decreases rapidly. On the other hand, the intensity of radiative heat flux increases from the core, and then it starts to decrease after passing the edge of the arc column: that is, there is a strong cooling mechanism inside the arc column by the radiation. Thus, the net heat energy to be gained by the flow, which is the joule heating energy minus the energy loss by radiation, is the largest at the edge of the arc column. As a result, the net heat energy strongly lifts up the temperature at the edge, which makes the temperature distribution flat in the arc column. Compared to a pure-air flow, the temperature of air–argon mixture can increase very easily, and it reaches the ionization temperature quickly because of the lower specific heat of argon. For this reason, the ionization of the argon flow is more active at the edge, which makes the arc column of air–argon gas thicker than that of air at the same energy.

Concerning operational data, the usage of present mixture model of changeable argon ratios did not make a noticeable difference from the result by the mixture model of the fixed argon ratio, since the region of the high argon ratio is confined at the region of the anode and the beginning of the constrictor.

B. Effect of Air Injection from Gaps

The constrictor tube consists of many disks approximately 1 cm in length, and the test gas is injected from the small gap between two

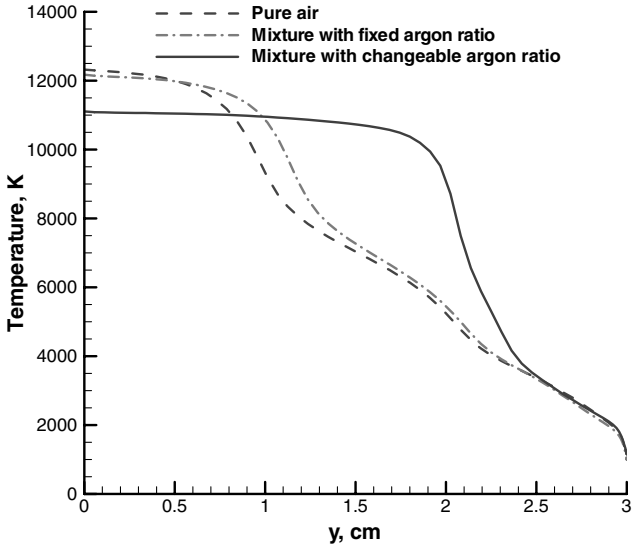

a) Beginning section of constrictor

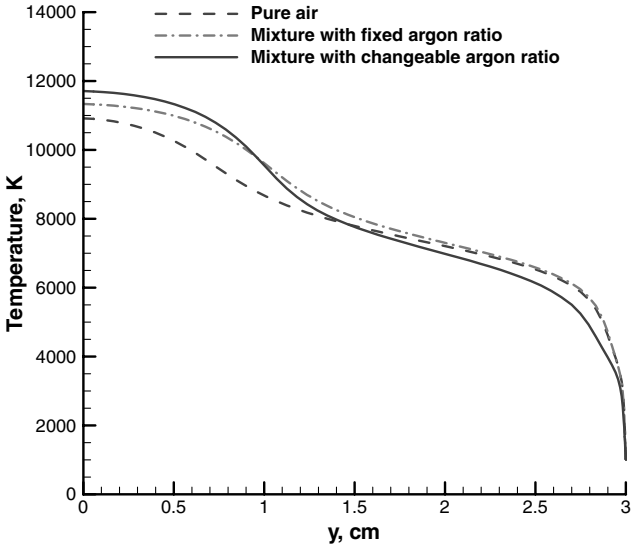

b) Middle section of constrictor

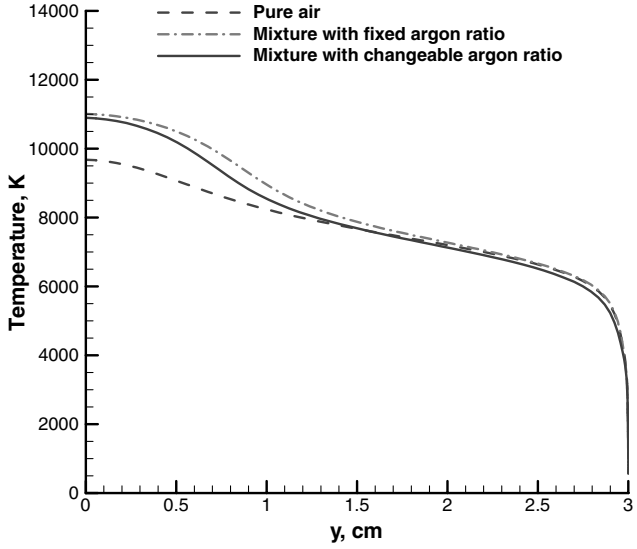

c) End section of constrictor

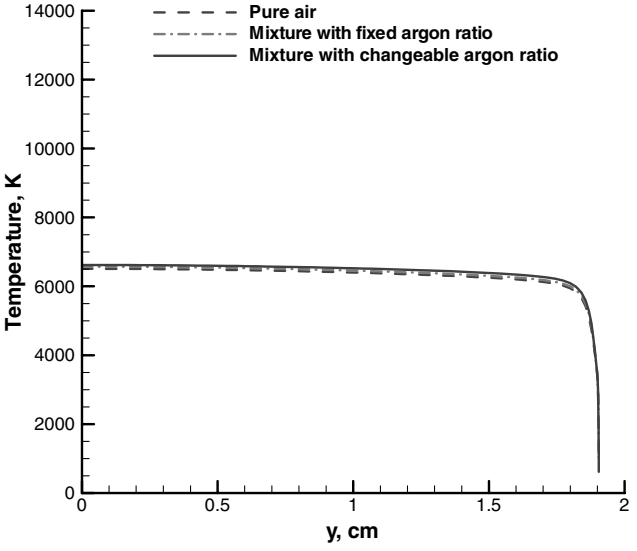

d) Section at nozzle throat

Fig. 8 Temperature distributions at cross sections of AHF arc heater.

disks. Thus, we divided the entire constrictor wall into the injection part between disks and the noninjection part on the disk to model the gas injection realistically. Figure 3a shows the wall boundary where the air was injected evenly through the entire surface of the constrictor wall, which was used in the previous studies [7–10]. Figure 3b shows the wall boundary where the air was injected through small gaps spaced out regularly on the constrictor wall, which was used in the present study.

To determine the appropriate gap size, convergence tests for gap size were performed. The interval between constrictor disks (i.e., a gap size) is several millimeters, and a large number of grid points along the surface of the constrictor are needed to consider the real size of gap in the numerical simulations. Therefore, for reduction of the computation time, proper lengths of a disk and a gap should be determined. The grid convergence tests were performed by using 200, 400, and 800 cell points along the surface of the constrictor, and the heat flux on disks of each case were almost same. On the other hand, the heat flux value was shown to depend on the ratio of the gas injection area to the total constrictor wall area.

Figure 9 shows total heat flux in terms of the ratios of the gas injection area on a disk placed around 213 cm from the starting point of the constrictor. In the figure, the average heat flux values on the

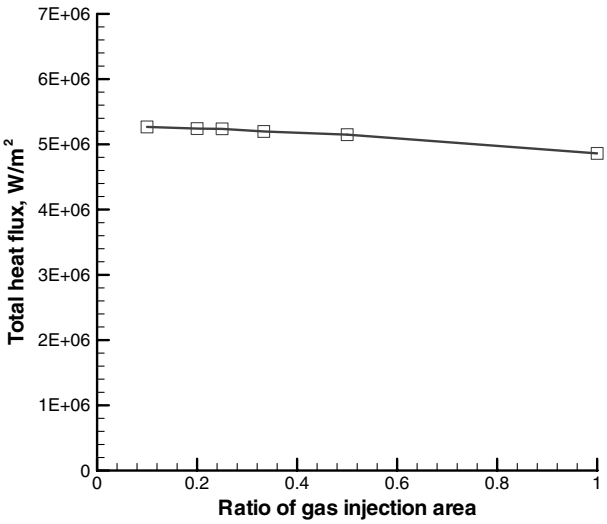

Fig. 9 Comparison of total heat flux on a disk of the downstream constrictor for the AHF arc heater.

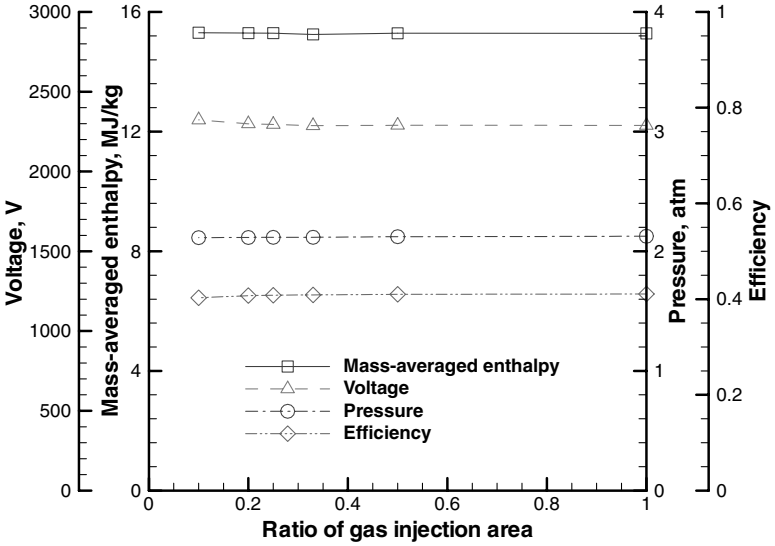

Fig. 10 Comparison of operational data in terms of the gas injection area ratio for the AHF arc heater.

disk converged, as the ratio of the gas injection area was less than 20%. Figure 10 shows the operational data in terms of the gas injection area ratio. The operational data did not change significantly with the gas injection area ratio, because the increase in heat flux on a disk is balanced by the loss of heat flux on a gap; that is, the total wall heat flux did not change significantly. Thus, 20% gas injection area ratio is thought to be reasonable to predict total heat flux on a disk as well as operational data.

Figure 11 shows the computational result for the heat flux on the AHF constrictor wall under a current of 1600 A and a mass flow rate of 0.1 kg/s. For these computations, a grid with 400 cell points along the surface of the constrictor was used, and the gas injection area was 20% of the total constrictor wall area. In the figure, the conductive heat flux for gas injection from the entire surface of the constrictor changed gradually along the surface of the constrictor. On the other hand, the conductive heat flux for gas injection from small gaps changed periodically, and there was a large difference in heat flux between the minimum and maximum values in a period, as shown in Fig. 11b. It is certain that this phenomenon is due to the difference of gas injection velocities normal to the surface on a disk and a gap. There is a strong injection velocity on a gap, but there is no velocity on a disk. Because the gas injection velocity makes the thermal boundary thicker, the conductive heat flux became lower on the gap. In contrast, the conductive heat flux became higher on the disk. As shown in Fig. 11a, about 16% of the conductive heat flux was increased. Since the heat flux to the disk is more important for the design of cooling system than the average heat flux, this kind of boundary condition is meaningful.

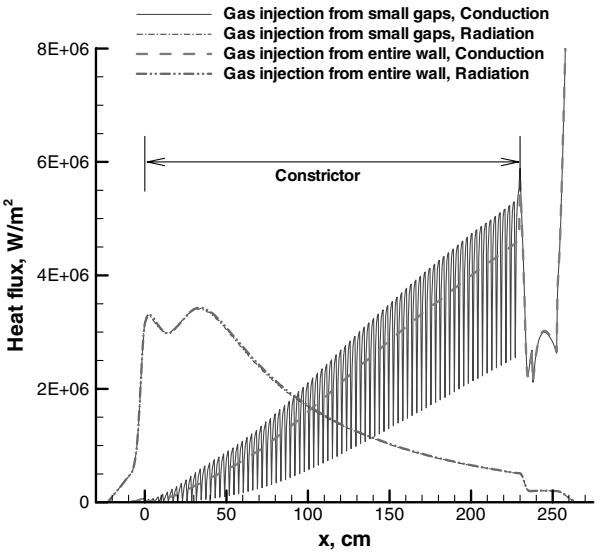

a) Heat fluxes on arc heater wall

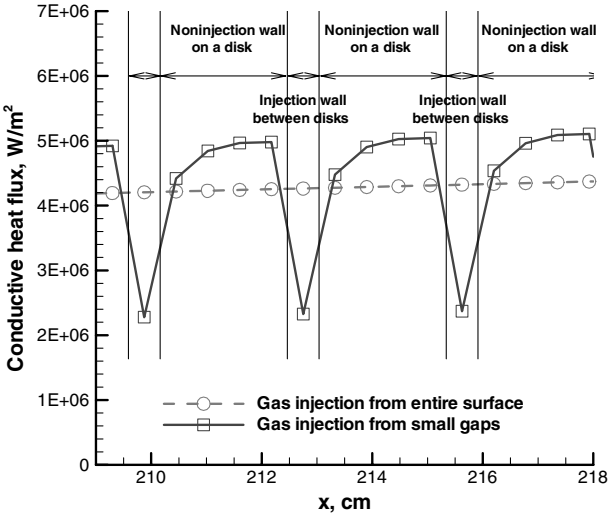

b) Conductive heat flux on downstream wall of constrictor

Fig. 11 Heat flux distributions on AHF arc-heater wall.

C. Comparison Between Computations and Experiments

1. Total Heat Flux Prediction for Panel Test Facility

Flow computation of the PTF was carried out. The total heat flux, which is the sum of conductive flux and radiative flux on the constrictor wall, was compared with experiment data. Taunk et al. [12] measured the total heat flux transferred to the wall from the flow with the calorimeter at two different positions: 25 and 213 cm from the starting point of the constrictor. They also compared these values with the results from the ARCFLO code. Sakai and Olejniczak [5] computed these flows using the ARCFLO3 code and compared the results with Taunk et al.'s experimental data [12]. In our study, computational and experimental results were compared in the same manner as Taunk et al.'s study.

The PTF is operated with the 20 MW segmented arc heater that produces a pressure range of 1 to 9 atm and an enthalpy level of 7 to 35 MJ/kg. The PTF arc heater has a constrictor diameter of 0.06 m and a length of 2.4 m. A semielliptical nozzle was used in Taunk et al.'s experiment [12]. Instead, a conical nozzle with the same

nozzle throat area was used in this study. The nozzle throat diameter was 0.035 m. There can be a small difference between the computed pressure and the realistic pressure due to a change in the configuration of the nozzle throat. However, differences in other thermodynamic properties, such as enthalpy and temperature, due to a change in the nozzle throat area are very small compared with the pressure difference [27].

Currents of 1500, 2000, and 2300 A were considered. In Taunk et al.'s experiment [12], argon at 0.0064 kg/s was injected from the upstream surface of the anode chamber. Figure 12 shows a comparison between experiment and computation of total heat flux on the constrictor wall at a current of 2300 A. The data are plotted in terms of cathode chamber pressures. In the figure, the computation using the ARCFLO code overestimated the total heat flux with too much error at the upstream location 25 cm from the starting point of the constrictor, but it fairly accurately predicted total heat flux at the downstream location 213 cm from the starting point of the constrictor. The ARCFLO3 computation underestimated the total heat flux with an average error of 24% at the upstream location, and it accurately predicted total heat flux with an n average error of 5% at the downstream location. On the other hand, our computation using the ARCFLO4 code is in good agreement with the experiment at both locations of the constrictor. The average error is 6% at the upstream location and 3% at the downstream location. Figure 13 shows the comparison of total heat flux at a current of 2000 A. The ARCFLO computation overestimated the total heat flux with significant error at the upstream location, and it deviated from the experiment data at the downstream location as the pressure increased. The ARCFLO3 code computation underestimated the total heat flux with an average error of 16% at the upstream location, but it accurately predicted the total heat flux at the downstream location. Similar to the results for a current of 2300 A, our ARCFLO4 code computation is in good agreement with the experiment at both locations of the constrictor. The average error is about 9% at the upstream location. Figure 14 shows the comparison of total heat flux for a current of 1500 A. The ARCFLO3 code computation underestimated with an average error of 33% at the upstream location, but it considerably overestimated the total heat flux at the downstream location when the mass flow was high. The computation using the ARCFLO4 code accurately predicted the total heat flux with an average error of 11% at the upstream location, but it predicted the total heat flux higher at the downstream location.

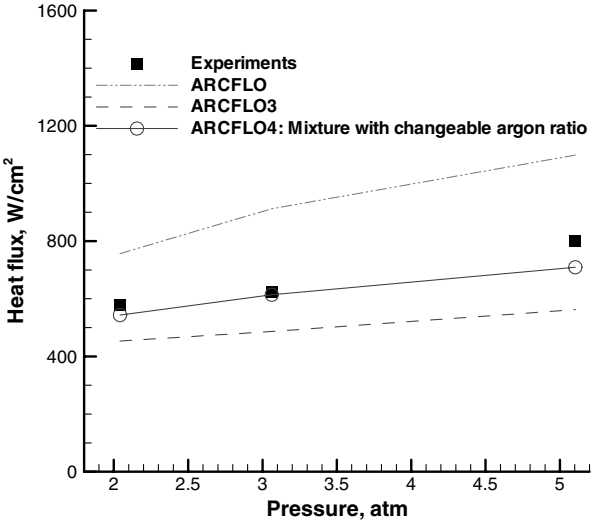

a) Upstream

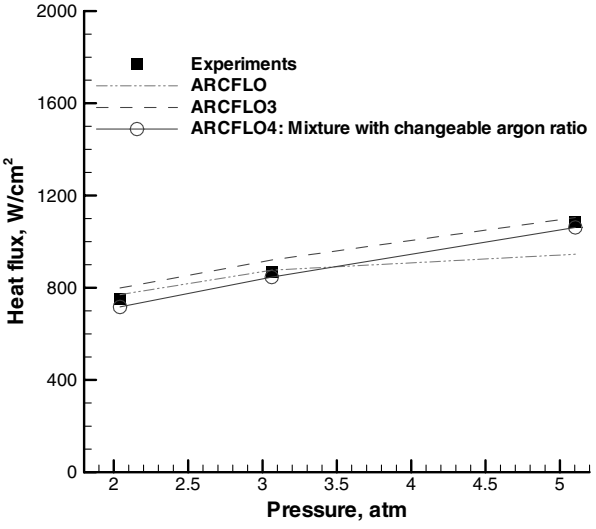

b) Downstream

Fig. 12 Comparisons of total heat flux at current of 2300 A for PTF arc heater.

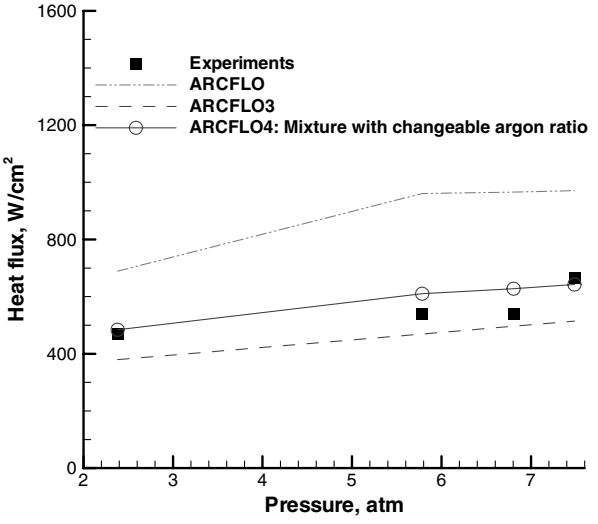

a) Upstream

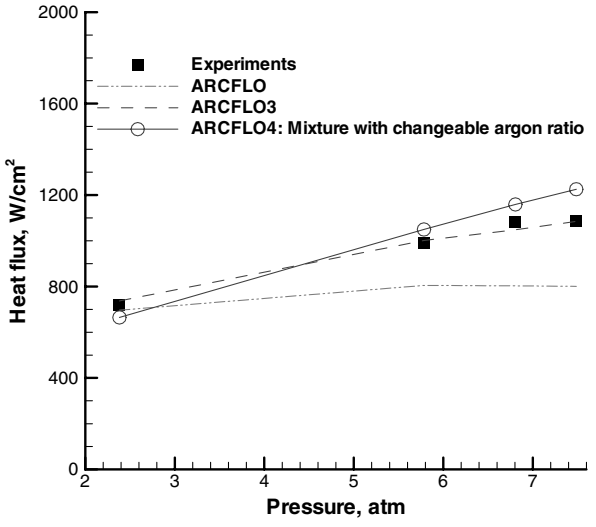

b) Downstream

Fig. 13 Comparisons of total heat flux at current of 2000 A for PTF arc heater.

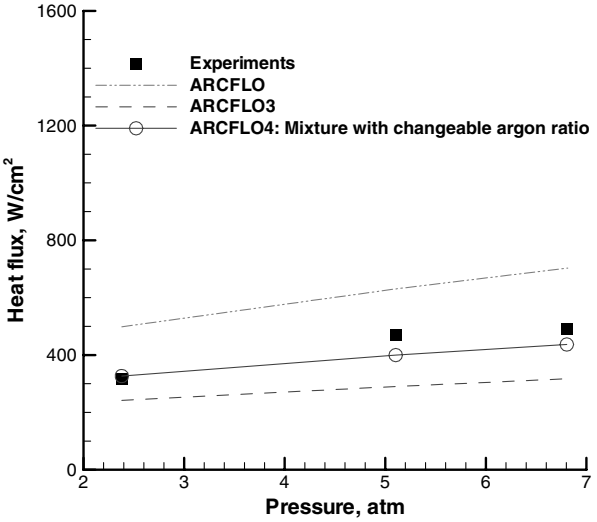

a) Upstream

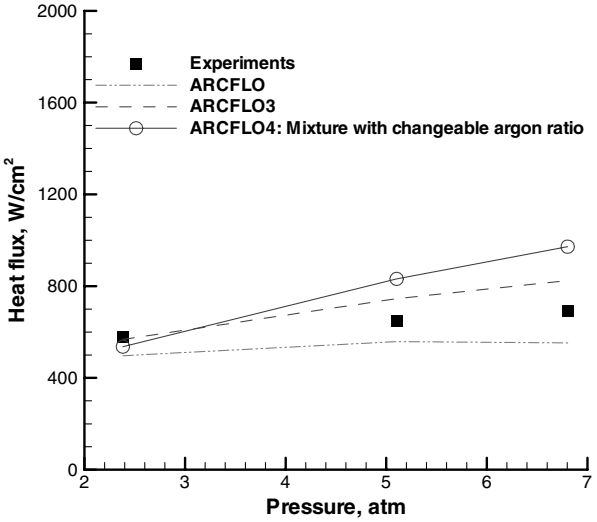

b) Downstream

Fig. 14 Comparisons of total heat flux at current of 1500 A for PTF arc heater.

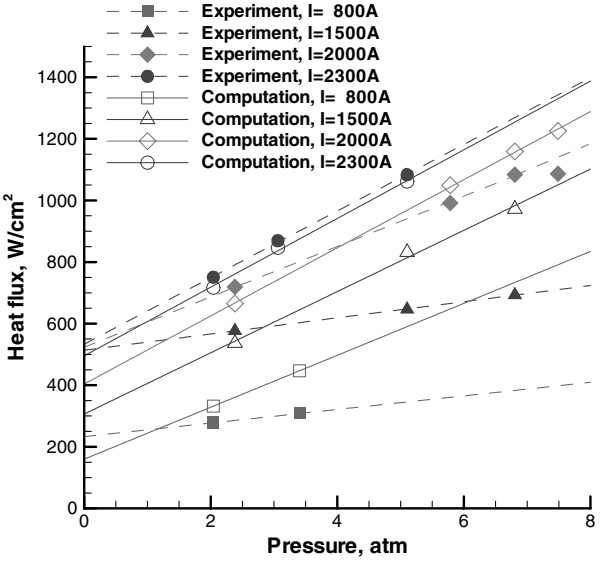

Fig. 15 Tendency of measured and computed heat flux on the downstream constrictor wall of the PTF arc heater.

At 1500 A, neither the ARCFLO3 code nor the ARCFLO4 code could predict the total heat flux at the downstream location. To determine the reason, measurements and computations were examined. Figure 15 shows all the measured and computed values for the total heat flux at the downstream location of the constrictor. The measurement values at a current of 800 A were added to compare the behavior of the total heat flux over a broad range of current conditions. The lines that pass through most of the measured and computed values at the same current were approximately straight. Using these lines, we found the tendency of the total heat flux for the computation as the current varied. The computed total heat flux was approximately proportional to the current at the same pressure. In contrast, it was not easy to find the tendency of the total heat flux for the measurement. The gradients of the lines for 800 and 1500 A are similar. However, they suddenly change for currents of 2000 and 2300 A. For currents of less than 1500 A, more detailed information on the experimental condition is needed.

Based on Figs. 12–14, our computation accurately predicts the total heat flux at the upstream location of the constrictor. From Fig. 11a, most of the total heat flux is generated by radiation at the upstream location [7,10]. Thus, our computation predicts radiation accurately by considering a realistic argon ratio, and the distributions of thermodynamic properties are more realistic than those in the previous computations [7–10].

2. *Operational Data and Centerline Enthalpy for Interaction Heating Facility*

The IHF is operated with a 60 MW segmented arc heater that produces a pressure range of 1 to 9 atm and an enthalpy level of 7 to 47 MJ/kg. The constrictor diameter and length are 0.08 and 3.9 m, respectively, and the nozzle throat diameter is 0.0603 m. Recently, Hightower et al. [28] carried out a series of arc-jet tests in the IHF, and Sakai and Olejniczak [5] computed those flows using ARCFLO3. In Hightower's experiment [28], argon at 0.04 kg/s was injected into both electrode chambers, and additional air was also injected from the rear part of the cathode chamber. In Sakai and Olejniczak's computation [5], the additional air was assumed to be a mixture of air–argon with the same argon ratio as the main working gas, and it was taken nominally to be 0.04 kg/s.

In our computation, the argon ratio of the injecting gas was controlled. Thus, the additional air injected into the cathode chamber was directly considered. The pure air at 0.04 kg/s was injected between the end of the cathode electrode and the entrance of the nozzle. In addition, argon at 0.02 kg/s was injected from the upstream surface of the anode chamber and the rest surface of the cathode chamber. Figure 16 shows the change in operational data plotted in terms of mass flow rates. We compared the additional air case with the nonadditional air case to investigate the effect of the additional air on an arc-heated flow. All our computations agreed with the experiment. In Fig. 16a, there is no significant difference in voltage between the additional air case and the nonadditional air case. In Fig. 16b, the mass-averaged enthalpy for the additional air case is lower than that for the nonadditional air case. The working gas mixed with the additional air was not heated by the arc, because the additional air was injected after the cathode. In Fig. 16c, as might be expected, the computed pressure for the nonadditional air case was underestimated slightly. Finally, Fig. 16d shows that the difference in efficiencies between the additional air case and the nonadditional air case was very small. Based on our computations, we confirmed that additional air decreased the mass-averaged enthalpy without changing the voltage and the efficiency.

The ratio of centerline enthalpy to average enthalpy is a very important physical parameter, because actual arc-jet experiments were carried out around the core region. Figure 17 shows this ratio at the nozzle throat for the IHF arc heater. The figure shows that these ratios are between 1.31 and 1.21 when additional air is not injected at the downstream location of the cathode chamber, and they are

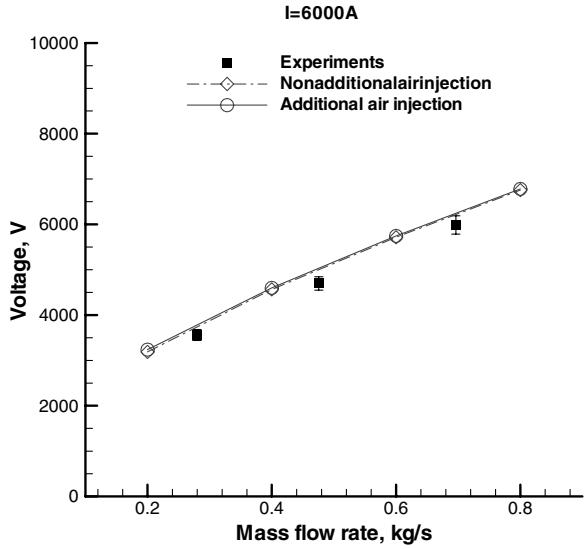

a) Voltage

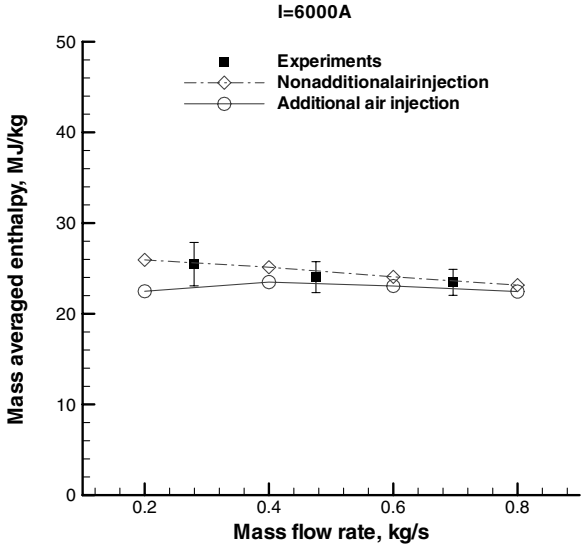

b) Mass averaged enthalpy

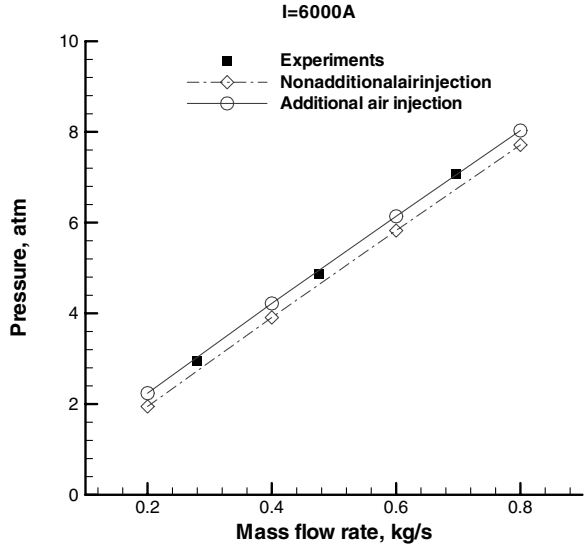

c) Pressure

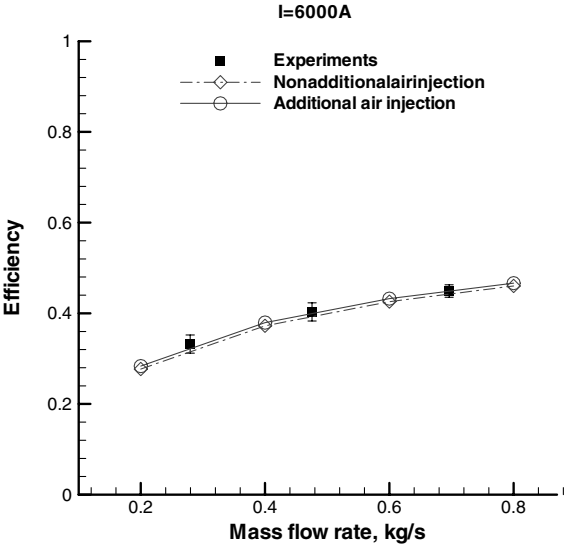

d) Efficiency

Fig. 16 Comparisons of operational data for IHF arc heater.

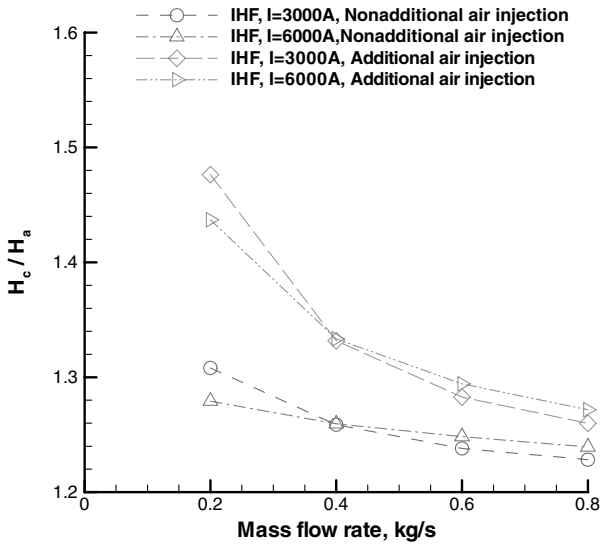

Fig. 17 Ratio of centerline enthalpy to mass-averaged enthalpy for IHF arc heater.

between 1.48 and 1.26 when the air is injected additionally at the downstream location of the cathode chamber. We confirmed that the ratio of centerline enthalpy to average enthalpy depends on the mass flow rate more than the current.

IV. Conclusions

The ARCFLO4 code was improved to simulate the flow of argon injected into electrode chambers simultaneously and air injected from the constrictor wall. The continuity equation of argon gas with a diffusion term was added to the original time-dependent axisymmetric Navier–Stokes equations, because the ratio of argon gas to the total working gas was changeable along the streamline in the arc heater. Thermodynamic and transport properties were calculated by considering 11 species including Ar and Ar^+ (N_2, O_2, Ar, N, O, NO, Ar^+, N^+, O^+, NO^+, and e^-) under the assumption of thermal equilibrium. Flow analysis of the 20 MW PTF, 20 MW AHF, and 60 MW IHF at the NASA Ames Research Center was conducted. The results show that the argon gas ratio changed dramatically as the gases flowed from the anode chamber to the nozzle throat, especially when the argon ratio was very high in the anode chamber and the beginning region of the constrictor. Compared with the previous studies that dealt with arc-heated flows with a fixed argon ratio, the

changeable argon ratio showed different distributions of the thermodynamic and transport properties in the arc heater. The enthalpy was much lower at the upstream region of the constrictor, because the argon ratio was very high and the specific heat of argon was much lower than air. Also, the upstream flow had a broad arc column where the temperature distribution remained high. This broad distribution of high temperature enhanced the radiation transferred to the wall. In addition, because of the distinction between the air-injected area and the disk area, a periodic distribution of conductive heat flux is observed. The total heat flux on a disk is about 16% higher than the averaged total heat flux, which is meaningful for the design of a new arc heater.

Finally, through comparison between computations and the experiments, it was confirmed that the computations accurately predict the total heat flux on the constrictor wall.

Acknowledgments

This research was supported by National Space Laboratory (S10801000121-08A0100-12110) program through the Korea Science and Engineering Foundation funded by the Ministry of Education, Science, and Technology. The authors wish to acknowledge this financial support. This work was also supported by grant KSC-2008-S02-0008 from the Korea Institute of Science and Technology Information. The authors would like to specially thank Chul Park for technical guidance at the Korea Advanced Institute of Science and Technology. The authors would also like to thank Takehara Sakai for the offer of his three-band radiation code at the Nagoya University.

References

[1] Nicolet, W. E., Shepard, C. E., Clark, K. J., Balakrishnan, A., Kesselring, J. P., Suchsland, K. E., and Reese, J. J., "Analytical and Design Study for a High-Pressure, High-Enthalpy Constricted Arc Heater," Arnold Engineering Development Center Rept._AEDC-TR-75-47, Manchester, TN, July 1975.

[2] Watson, V. R., and Pegot, E. B., "Numerical Calculations for the Characteristics of a Gas Flowing Axially Through a Constrictor Arc," NASA TN_D-4042, June 1967.

[3] Kim, K. H., Rho, O. H., and Park, C., "Navier–Stokes Computation of Flows in Arc Heaters," *Journal of Thermophysics and Heat Transfer*, Vol. 14, No. 2, 2000, pp. 250–258. doi:10.2514/2.6516

[4] Sakai, T., and Olejniczak, J., "Navier–Stokes Computations for Arcjet Flows," AIAA Paper 2001-3014, Jun. 2001.

[5] Sakai, T., and Olejniczak, J., "Improvement in a Navier–Stokes Code for Arc Heater Flows," AIAA Paper 2003-3782, Jun. 2003.

[6] Sakai, T., "Computational Simulation of High-Enthalpy Arc Heater Flows," *Journal of Thermophysics and Heat Transfer*, Vol. 21, No. 1, 2007, pp. 77–85. doi:10.2514/1.26083

[7] Lee, J. I., Kim, C., and Kim, K. H., "Accurate Computations of Arc-heater Flows Using Two-Equation Turbulence Models," *Journal of Thermophysics and Heat Transfer*, Vol. 21, No. 1, 2007, pp. 67–76. doi:10.2514/1.25495

[8] Lee, J. I., Kim, C., Kim, K. H., and Rho, O. H., "Investigation of Turbulent Flow Effects in Segmented Arc-Heater," AIAA Paper 2005-0172, Jan. 2005.

[9] Lee, J. I., Kim, C., and Kim, K. H., "Numerical Modeling for the Accurate Computations of Arc-Heater Flows," *ECCOMAS CFD 2006 Conference* [CD-ROM], edited by E. Oñate, J. Périaux, and P. Wesseling, Delft Univ. of Technology, The Netherlands, Sept. 2006.

[10] Lee, J. I., Han, S. H., Kim, C., and Kim, K. H., "Analysis of Segmented Arc-Heater Flows with High Argon Concentration," *Journal of Thermophysics and Heat Transfer*, Vol. 22. No. 2, 2008, pp. 187–200. doi:10.2514/1.33623

[11] Jones, W. P., and Launder, B. E., "The Prediction of Laminarization with a Two-Equation Model of Turbulence," *International Journal of Heat and Mass Transfer*, Vol. 15, No. 2, 1972, pp. 301–314. doi:10.1016/0017-9310(72)90076-2

[12] Taunk, J. S., Shepard, C. E., Carrasco, A., "Design and Verification of a Copper Disk for Radiation Measurements in the Constrictor Region of an Arc Jet," Instrument Soc. of America Paper 94-3025, Baltimore MD, 1994.

[13] Terrazas-Salinas, I., and Cornelison, C., "Test Planning Guide for ASF Facilities," NASA Ames Research Center Rept. A029-9701-XM3 Rev. B, Moffett Field, CA, March 1999.

[14] Kim, K. H., Kim, C., and Rho, O. H., "Methods for the Accurate Computations of Hypersonic Flows: I. AUSMPW+ Scheme," *Journal of Computational Physics*, Vol. 174, No. 1, Nov. 2001, pp. 38–80. doi:10.1006/jcph.2001.6873

[15] Han, S. H., Lee, J. I., and Kim, K. H., "Accurate and Robust Pressure Weight Advection Upstream Splitting Method for Magnetohydrodynamics Equations," *AIAA Journal*, Vol. 47, No. 4, 2009, pp. 970–981. doi:10.2514/1.39375

[16] Jameson, A., and Yoon, S., "Lower-Upper Implicit Schemes with Multiple Grids for the Euler Equations," *AIAA Journal*, Vol. 25, No. 7, 1987, pp. 929–935. doi:10.2514/3.9724

[17] Gordon, S., and McBride, B. J., "Computer Program for Calculation of Complex Chemical Equilibrium Compositions and Applications: I. Analysis," NASA, Ref. Publ. 1311, Oct. 1994.

[18] McBride, B. J., Zehe, M. J., and Gordon, S., "NASA Glenn Coefficients for Calculating Thermodynamic Properties of Individual Species," NASA TP 2002-211556, Sept. 2002.

[19] Gupta, R. N., Yos, J. M., Thompson, R. A., and Lee, K. P., "A Review of Reaction Rates and Thermodynamic and Transport Properties for an 11-Species Air Model for Chemical and Thermal Nonequilibrium Calculations to 30,000 K," NASA RP-1232, Aug. 1990.

[20] Yos, J. M., "Transport Properties of Nitrogen, Hydrogen, Oxygen, and Air to 30,000 K," AVCO Corp. TM 63-7, Wilmington, MA, Mar. 1963.

[21] Hirschfelder, J. O., Curtiss, C. F., and Bird, R. B., *Molecular Theory of Gases and Liquids*, Wiley, New York, 1967.

[22] Park, C., Jaffe, R. L., and Partridge, H., "Chemical-Kinetic Parameters of Hyperbolic Earth Entry," *Journal of Thermophysics and Heat Transfer*, Vol. 15, No. 1, 2001, pp. 76–90. doi:10.2514/2.6582

[23] Kim, J. G., Oh, J. K., and Park, C., "A High Temperature Elastic Collision Model for DSMC Based on Collision Integrals," AIAA Paper 2006-3803, June 2006.

[24] Whiting, E. E., Park, C., Liu, Y., Arnold, J. O., and Paterson, J. A., "NEQAIR96, Non-Equilibrium and Equilibrium Radiative Transport and Spectra Program: User Manual," NASA, Ref. Pub. 1389, Dec. 1996.

[25] Wilcox, D. C., *Turbulence Modeling for CFD*, 2nd ed., DCW Industries, La Canada, CA, 1998, pp. 119–122.

[26] Menter, F. R., "Two-Equation Eddy-Viscosity Turbulence Models for Engineering Applications," *AIAA Journal*, Vol. 32, No. 8, Nov. 1994, pp. 1598–1605. doi:10.2514/3.12149

[27] Lee, J. I., and Kim, K. H., "Numerical Parameter Study of Low Electric Power Segmented Arc Heaters," AIAA Paper 2010-0230, Jan. 2010.

[28] Hightower, T. M., Balboni, J. A., MacDonald, C. L., Anderson, K. F., and Martinez, E. R., "Enthalpy by Energy Balance for Aerodynamic Heating Facility at NASA Ames Research Center Arc Jet Complex," *48th International Instrumentation Symposium*, Instrumentation, Systems, and Automation Soc., Research Triangle Park, NC, May 2002.